

Motion-Driven Neural Optimizer for Prophylactic Braces Made by Distributed Microstructures

ANONYMOUS AUTHOR(S)

SUBMISSION ID: 851*

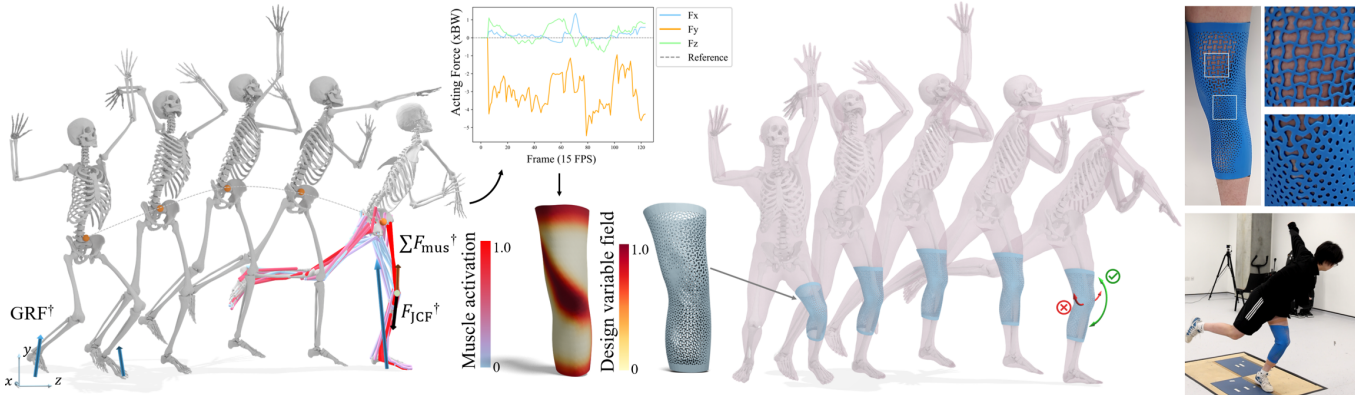


Fig. 1. Given an input motion paired with ground reaction forces (GRFs), our approach produces a controlled distribution of elasticity physically realized by microstructures for prophylactic braces. The time-variant load given by kinetic analysis is plotted in the middle, where the frames have been downsampled to 15 fps and the acting forces are normalized to body weight (the testing participant weighs 64 kg). With the help of the optimized brace design, the frontal angles can be effectively reduced while keeping the flexibility of motion throughout the range within sagittal plane.

[†] The force vectors include the GRF, the joint-contact force and the muscle forces are all scaled down by 0.5× for visualization purposes.

Joint injuries, and their long-term consequences, present a substantial global health burden. Wearable prophylactic braces are an attractive potential solution to reduce the incidence of joint injuries by limiting joint movements that are related to injury risk. Given human motion and ground reaction forces, we present a computational framework that enables the design of personalized braces by optimizing the distribution of microstructures and elasticity. As varied brace designs yield different reaction forces that influence kinematics and kinetics analysis outcomes, the optimization process is formulated as a differentiable end-to-end pipeline in which the design domain of microstructure distribution is parameterized onto a neural network. The optimized distribution of microstructures is obtained via a self-learning process to determine the network coefficients according to a carefully designed set of losses and the integrated biomechanical and physical analyses. Since knees and ankles are the most commonly injured joints, we demonstrate the effectiveness of our pipeline by designing, fabricating, and testing prophylactic braces for the knee and ankle to prevent potentially harmful joint movements.

CCS Concepts: • Do Not Use This Code → Generate the Correct Terms for Your Paper; Generate the Correct Terms for Your Paper; Generate the Correct Terms for Your Paper; Generate the Correct Terms for Your Paper.

Permission to make digital or hard copies of all or part of this work for personal or classroom use is granted without fee provided that copies are not made or distributed for profit or commercial advantage and that copies bear this notice and the full citation on the first page. Copyrights for components of this work owned by others than ACM must be honored. Abstracting with credit is permitted. To copy otherwise, or republish, to post on servers or to redistribute to lists, requires prior specific permission and/or a fee. Request permissions from permissions@acm.org.

ACM SIGGRAPH Asia 2024, December 03–06, 2024, Tokyo, Japan

© 2018 Association for Computing Machinery.

ACM ISBN 978-1-4503-XXXX-X/18/06...\$15.00

<https://doi.org/XXXXXXX.XXXXXXX>

Additional Key Words and Phrases: Motion driven, Computational design, Microstructures, Neural network, Topology optimization

ACM Reference Format:

Anonymous Author(s). 2018. Motion-Driven Neural Optimizer for Prophylactic Braces Made by Distributed Microstructures. In . ACM, New York, NY, USA, 10 pages. <https://doi.org/XXXXXXX.XXXXXXX>

1 INTRODUCTION

In the realm of sports and recreational activities, the potential for injury presents a universal challenge. A well-designed prophylactic brace needs to provide thorough protection without constraining performance. Many current simulation-based design methods (e.g., [Andersen and Rasmussen 2023]) employ a two-stage process by iteratively updating the input of the biomechanical analysis (i.e., the brace designs and the reaction forces) and the input loads of the physical analysis (i.e., the action forces). They require separate phases for initial development and subsequent integration along with manual iterations, which makes it challenging to benefit from the functionality of topology optimization for generating distributed elasticity [Liu et al. 2023a]. To overcome this limitation, we propose a computational pipeline that enables time-variant topology optimization equipped with kinematics and kinetics analysis (Fig.1). The effectiveness of our approach has been verified by physically fabricated braces through try-on tests and motion evaluations.

While more material may provide more support, distributing coverings over highly mobile regions might restrict mobility [Vechev et al. 2022a]. Our design strategy aims for a balance: crafting a prophylactic brace that offers precise kinematics control of limiting undesired rotation (typically in the frontal plane) while preserving

range of motion within the sagittal plane to execute movements safely. To achieve this, we consider both movement patterns (kinematics) and the forces involved (kinetics) in the design with integrated biomechanical and physical analyses. We propose a design optimization for distributing elasticity, fabricated as microstructures in a hyperelastic material. The optimization is parameterized in a neural network with a self-learning process. We implement a carefully designed set of losses combined with integrated biomechanical and physical analyses. The result is a physical brace providing tailor-made prevention and preservation throughout the motion sequence. In summary, our contributions are as follows:

- We investigate a closed-loop differentiable framework that can systematically optimize a customized brace design by integrated biomechanical analysis, physics analysis, and time-variant topology optimization (Sec. 3).
- We developed a formulation that effectively generates distributed microstructures based on the optimized neural function to achieve the desired elasticity distribution (Sec. 4).

We have used our pipeline to design prophylactic braces and showcase the applicability of the method through designs with different joint dynamics and conditions.

2 RELATED WORK

2.1 Computational Design of Prophylactic Wearables

Prophylactic bracing is a widely used and cost-effective intervention for preventing the physical consequences of joint injuries. In particular, prophylactic knee braces are designed to control knee motion that is thought to increase the risk of anterior cruciate ligament (ACL) and other soft tissue injuries at the knee [Tuang et al. 2023]. According to Tuang et al. [2023], reducing peak knee abduction (valgus) angles in the coronal (frontal) plane can potentially lower the risk of noncontact ACL injury. In the sagittal plane, the goal is typically to promote greater knee flexion since landing with a more extended knee, with a reduced knee flexion angle range, can increase the load on the ACL and, consequently, a higher risk of ACL injury [Myer et al. 2011]. At the ankle, prophylactic braces or taping is meant to reduce the incidence of ankle injuries such as lateral ankle sprains (e.g., [Farwell et al. 2013; Gross and Liu 2003; Hagan et al. 2024; Verhagen and Bay 2010]). These biomechanical insights guide our objective design of precise kinematics control over different planes to ensure joint stability.

Biomechanical simulation tools, such as AnyBody [Andersen and Rasmussen 2023] and OpenSim [Delp et al. 2007], offer a promising avenue for improving the design and optimization with the finite element analysis (FEA), enabling customization and cost-effective simulations. We employ the biomechanical analysis library provided by OpenSim to realize an end-to-end computational pipeline of motion-driven optimization.

In computational design, research has been conducted for decades to provide compression with customized shape of braces (e.g., [Wang and Tang 2007]). Recently, Zhang and Kwok [2019] applied the topology optimization technique to design custom compression casts/braces on two-manifold mesh surfaces to reduce weight and improve performance. Jiang et al. [2022] demonstrated a design

of a customized ankle brace that has a tunable mechanical performance with tailored stiffness by machine learning integrated design. Vechev et al. [2022c] demonstrated the design of kinesthetic garments, which are passively reinforced garments designed to resist a single motion. They also proposed an automatic optimization method to design connecting structures that efficiently resist a range of pre-defined body motions on demand [Vechev et al. 2022b]. However, these existing approaches have yet to consider the influence of reaction forces generated by varied designs of braces on the biomechanical model.

2.2 Topology Optimization

Time-variant topology optimization is crucial for optimizing structures under time-dependent conditions. Unlike the traditional methods developed for static problems that have been intensively studied, only a few studies can be found in the literature on this topic (e.g., [Jensen 2009; Wang et al. 2020]). Their strategy of space-time extension is employed in our pipeline to formulate the motion-driven design optimization problem.

Topology optimization for microstructures was introduced by combining numerical homogenization in [Sigmund 1994]. Many algorithms have since been developed based on this method to optimize the unit geometry of microstructures for desired effective performance, including heterogeneous materials [Torquato 2010], functionally graded properties [Radman et al. 2013], and two-scale designs with multi-material microstructures [Zhu et al. 2017]. A strategy similar to [Chen et al. 2018] is employed in our pipeline to generate the distributed microstructures using the popular Solid Isotropic Material with Penalization (SIMP) approach.

Recently, the computation of topology optimization has started to employ Neural Network (NN) techniques to gain the benefit of NN-based computational pipelines such as the auto-differentiation technique and the highly parallel computing power. Zhang et al. [Zhang et al. 2021] and Chandrasekhar et al. [Chandrasekhar and Suresh 2021] explored the method that directly optimized the density field alongside the update of NN's weights and bias, which was recently extended to designing microstructure cells [Sridhara et al. 2022]. Another benefit of NN-based computation is the functional and continuous representation of the design field, which facilitates meshless analysis and optimization (e.g., [Zehnder et al. 2021]). Unlike methods that employ deep neural networks, recent work by Qian et al. [Qian et al. 2023] uses a single layer of Gaussian activation functions to achieve NN-based topology optimization. Due to the Gaussian functions' capability to capture nonlinear features, fewer neurons (i.e., design variables) need to be optimized, leading to faster convergence. We adopt a similar network architecture.

3 MOTION-DRIVEN NEURAL OPTIMIZER

We introduce a topology design pipeline for prophylactic braces integrated with biomechanical analysis. Our pipeline produces an optimized elasticity distribution given time-variant loads acting on the human body. An overview can be found in Fig. 2.

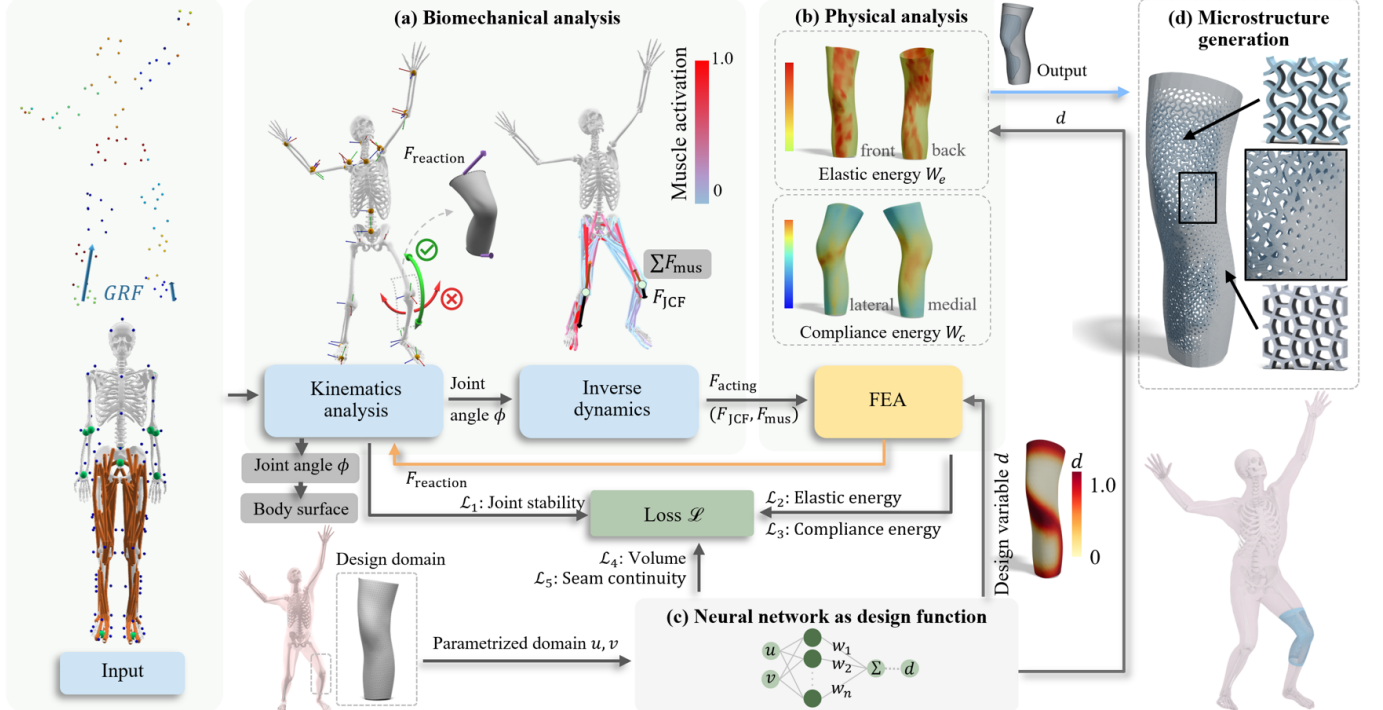


Fig. 2. Overview of our computational pipeline, which includes four major parts: (a) biomechanical analysis, (b) physical analysis, (c) the *neural network* (NN) based representation of design function, and (d) microstructure generation. From the input sequence of motion and paired ground reaction forces (GRFs), we first conduct a preprocessing step to determine the corresponding joint angle, the muscle forces, and the design domain as the body surface with the help of a predefined musculoskeletal model. These terms remain unchanged throughout the optimization (as marked in gray blocks). Our topology optimization process, informed by the time-variant forces F_{acting} given by the biomechanical analysis (a) and governed by the FEA-based physical analysis (b), iteratively updates the NN’s weights (c) as design variables to change the distribution of stiffness on a brace while minimizing the compliance energy W_c . In our pipeline, the biomedical analysis and the physical analysis are closely coupled since the reaction force exerted by the braces will further impact the kinematics. The forces generated by a brace at its upper and lower boundaries F_{reaction} are applied to the femur and tibia bones, respectively, prompting updates to the joint contact forces for subsequent analysis. The distributed microstructures for realizing the optimized distribution of stiffness can be generated by first computing the distribution of elastic energy W_e and then filling the regions in low and high elastic energies with the well-blended firm (displayed in gray) and soft microstructures (displayed in blue) respectively.

3.1 Data Processing

3.1.1 Inputs. The paired motion capture (MoCap) and ground reaction forces (GRF) are used as the input for defining movement and the external force resulting from the body’s contact with the ground [Han et al. 2023]. We customize a musculoskeletal model (Fig. 3(a)) from [Bedo et al. 2020; Lerner et al. 2015] with $N = 41$ degrees of freedom (DoF) including 3 DoFs for each knee. The musculoskeletal model also contains 80 Hill-type muscles to evaluate the muscle forces. We customize the locations of markers to ensure alignment with body positions, thereby enhancing the accuracy of the kinematic analysis.

3.1.2 Kinematics and optimization objectives. From the MoCap and GRF data, we employ OpenSim [Delp et al. 2007] and AddBiomechanics [Werling et al. 2023] to calculate the joint angles from marker trajectories by inverse kinematics, with $\phi \in \mathbb{R}^N$ representing the joint angles. Through optimization, we track joint angle changes in response to the additional reaction force exerted by the braces. We aim to restrict the movement in the frontal plane by minimizing the

abduction/adduction at the knee and inversion/eversion at the ankle, as they can lead to joint instability and injuries like anterior cruciate ligament (ACL) tears or ankle sprain. Conversely, maintaining a full range of motion in the sagittal plane is essential for safeguarding the human body, particularly during landing movements; these sagittal angles are the ones we strive to preserve.

3.1.3 Body reconstruction. Extracting the outer skin surface directly from a musculoskeletal model is challenging due to complex anatomy and dynamic deformation introduced by motions. To address this, we employ the SKEL model (β, \mathbf{q}) [Keller et al. 2023], which defines a parametric body model with corresponding skin and skeleton meshes. $\beta = [\beta_1, \dots, \beta_{10}]$ is the shape parameters, and $\mathbf{q} \in \mathbb{R}^{46}$ is the pose parameters representing 46 DoFs of the articulated body. We select some specific regions from the extracted body surface to construct the design domain (Fig. 2). This allows us to analyze the impacts of motion / forces acting on the targeted areas.

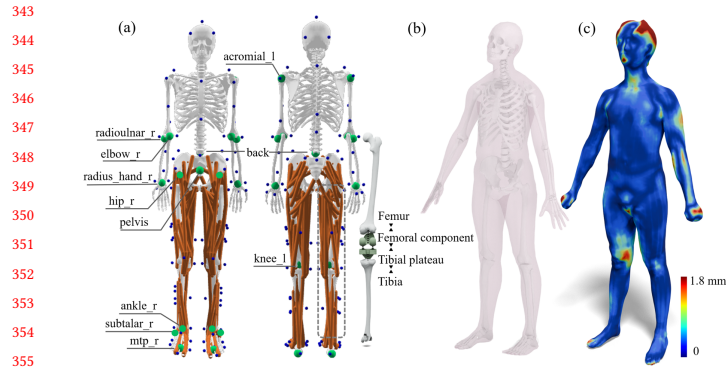


Fig. 3. (a) Overview of the biomechanical model and the marker layout alignment for kinematics and kinetics analysis, where we customize a detailed knee compartment model [Bedo et al. 2020; Lerner et al. 2015] by equipping both knees with three DoFs and adjusting the marker layout to accommodate more detailed kinematics. (b) From the musculoskeletal model, we extract the outer skin surface by fitting it to the SKEL model (β , q) [Keller et al. 2023], where the shape parameters β are obtained from the scanned body as shown in (c) to estimate detailed deformations. The color map measures the shape approximation error between the scanned and updated SKEL bodies.

3.1.4 Parametrization for brace design. Customized braces can be simplified as two-manifold designs on a surface with uniform thickness. These designs are parameterized onto a domain as $(u, v) \in [0, 1]$ using the least squares conformal maps [Lévy et al. 2023]. This reduces the dimensionality of the design domain, making it easier to conduct physical analysis and the generation of distributed microstructures. For taking FEA, the domain is tessellated into a triangular mesh \mathcal{M} . Note that the initial relaxed state of the body mesh instead of a deformed mesh is employed for parameterization in our implementation. Moreover, introducing a cutting line is necessary when parameterizing a brace surface resembling a cylinder onto a two-dimensional plane. Constraints are added during the optimization to ensure the design variables at both sides of the cutting line are consistent.

3.2 Biomechanical Analysis

During human motion, forces and torques (or moments) acting across a joint are derived from external (ground reaction forces) and internal (body weight, muscle forces, soft tissue forces, joint contact forces) sources. At any given instant in time, the dynamic equilibrium is defined as $\sum \mathbf{F} = m\mathbf{a}$ and $\sum \mathbf{M} = I\boldsymbol{\alpha}$ with body segments' mass m , acceleration \mathbf{a} , inertia I , and angular acceleration $\boldsymbol{\alpha}$. Braces can generate reaction forces as additional external sources that alter the magnitude of other components of the dynamic equilibrium.

3.2.1 Joint contact forces. A joint contact force (F_{JCF}), as shown in Fig. 4(a), represents the actual load transmitting between bones within a joint. While directly measuring the contact force is difficult, we model the contact with [Delp et al. 2007] similar to [Bedo et al. 2020; Lerner et al. 2015] as shown in Fig. 3(a) to extract compressive force acting on the tibia bones for the knee and on the talus bones for the ankle joints. We compute F_{JCF} with *joint reaction analysis*

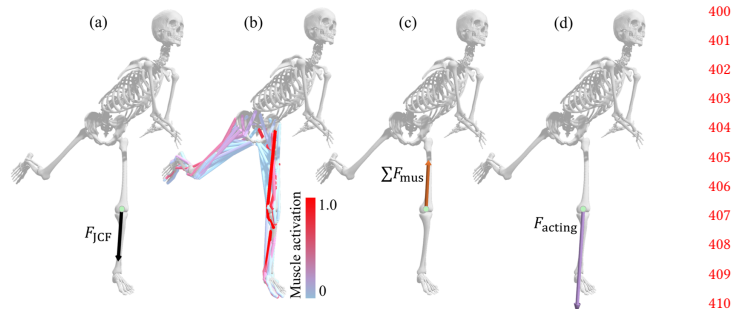


Fig. 4. We show the kinetic analysis of an example left knee joint during the tennis serve motion, specifically at the landing pose. The biomechanical dynamic analysis can estimate (a) the joint contact forces, F_{JCF} , acting on the tibia bone, (b) the muscle activations and (c) the sum of muscle forces ΣF_{mus} . The acting force (d) can then be computed as Eq. (1), which serves as the load input for the integrated FEA. Our optimizer considers the entire sequence of a complex motion, such as tennis serving, which includes several critical phases such as deep bending knees, jumping, and landing.

(JRA) [Delp et al. 2007] given the kinematics and the external loads defined by GRF and the brace reaction forces.

3.2.2 Muscle forces. Muscles play a crucial role in supporting and stabilizing joints. A prophylactic brace can supplement muscle action by sharing the load. Following [Delp et al. 2007] and [Feng et al. 2023], we model the muscle as polylines. Muscle activation falling in the range of $[0, 1]$ determines the level of contraction in a muscle, which is used to estimate the muscle forces. During the computation, we only consider the muscles that traverse through the joint. The direction of the net muscle force is determined by considering each muscle line that is involved. We denote the sum of the muscle forces as ΣF_{mus} .

3.2.3 Overall acting force. The overall input forces for FEA are the net loads acting on the joint, accounting for both passive (due to the joint and body weight) and active (due to muscle support) components. Specifically, we define the force as follows, and the acting force serves as time-variant loads for FEA:

$$F_{acting} = F_{JCF}(F_{GRF}, F_{reaction}) - \sum F_{mus} \quad (1)$$

With these boundary conditions, we can formulate the optimization problem to compute the optimized topology for distributed elasticity.

3.3 Motion-driven Topology Design

Traditional topology optimization algorithms focus on spatial design domains, such as density fields. However, they may not be directly applicable or efficient for addressing time-variant loading problems arising from kinesthetic brace designs. This limitation stems from the high computational cost associated with variable-time nonlinear physical models and the non-convex nature of the design space [Cai et al. 2023]. Developing or adapting algorithms that can efficiently navigate this complex landscape remains a significant challenge. Therefore, we integrate the space field with the motion frame, concurrently addressing them through discretization and optimization within a framework.

3.3.1 *Time-variant Topology Optimization Model.* By borrowing the concept of the density-based SIMP method [Sigmund 2001], we construct the time-variant topology optimization driven by action forces obtained from the kinematics and kinetics analysis. The design domain $d(u, v)$ (similar to ‘density’ concept in SIMP) is represented by a neural network (NN), which is parameterized by the network coefficients θ . For numerical computation, the SIMP-like optimization is conducted by tessellating the whole domain into finite elements. The design variable d_e in each element e is chosen by the field value at the center of e , where different values of d_e will be mapped to different volume fractions and mechanical properties. In motion-involved scenarios, loads and body surface can change with time; the time-variant loads can be represented as $F(t)$ with a total of N_t frames sampled at the rate of 15 fps as shown in Fig.1. The walking motion shown in Fig. 9 is sampled at 60 fps.

The time-variant topology optimization problem can then be solved by minimizing the ‘worst’ compliance energy as:

$$\begin{aligned} \min_d \max_{\{t_i\}} & \left\{ \frac{1}{2} \mathbf{U}^T \mathbf{K}(d) \mathbf{U} \right\} \\ \text{s.t. } & \mathbf{K}(d) \mathbf{U} = \mathbf{F}_{\text{acting}}(t_i), \\ & \sum_{e=1}^{N_l} (f_V(d_e) \cdot V_e) \leq V_0, \\ & e = 1, 2, \dots, N_l, i = 1, 2, \dots, N_t, \end{aligned} \quad (2)$$

where N_l is the number of elements, \mathbf{K} and \mathbf{U} are the global stiffness matrix and nodal displacement vector for FEA. The FEA is conducted by planer elements equipped with the rotation matrix between 3D surface and its corresponding region in the u, v -domain. Note that the boundary condition of fixing the nodes on the boundaries of a brace needs to be imposed for FEA. V_0 is the allowed maximal volume, V_e is the volume of element e , \mathbf{k}_0 is the elemental stiffness matrix, and $\mathbf{F}_{\text{acting}}$ indicates the applied nodal force, and d_e is the design variable of the element e . The discrete compliance on each element e can be defined as $W_c = f_E(d_e) \cdot \mathbf{u}_e^T \cdot \mathbf{k}_0(t_i) \cdot \mathbf{u}_e$ with \mathbf{u}_e being the nodal displacement of element e . $f_E(\cdot)$ and $f_V(\cdot)$ are the functions of the Young’s modulus and the volume ratio related to the design function $d(\cdot)$. We further employ p -norm method to approximate the maximum compliance across all the N_t frames as given in Table 1 of Sec. 5.

The reaction force can be computed by the displacement $\mathbf{U}(t_i)$ and the acting force $\mathbf{F}_{\text{acting}}(t_i)$ as

$$\mathbf{F}_{\text{reaction}}(t_i) = \mathbf{K}(d) \mathbf{U}(t_i) - \mathbf{F}_{\text{acting}}(t_i) \quad (3)$$

This reaction force serves as the brace support and acts back to the body to update the joint angles ϕ and the joint contact forces \mathbf{F}_{JCF} sequentially with the kinematics and joint reaction analysis introduced above.

3.3.2 *Elastic Energy Based Segmentation.* We employ elastic energy density to estimate the degree of local deformation on the time-variant surfaces of a human body. To alleviate the constrained movement caused by the wrapping of braces, we aim to minimize the total elastic energy on the prophylactic brace. The distribution of elastic energy can be commonly evaluated by the design function $d(\cdot)$ and the deformation of elements on a brace among different

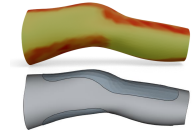
frames. Specifically, given $\mathbf{G}_e(t_i)$ as the deformation gradient [Sumner and Popović 2004] of the element e at the time frame t_i w.r.t. its rest shape, the elastic energy W_e at every element can be evaluated by using the classical compressible neo-Hookean model [Bonet and Wood 2008] as

$$W_e = \max_{\{t_i\}} \left\{ \frac{\mu_e}{2} (I_e(t_i) - 2) - \mu_e \log A_e(t_i) + \frac{\lambda_e}{2} (\log A_e(t_i))^2 \right\} \quad (4)$$

where $I_e = \text{tr}(\mathbf{C}_e)$ is the first invariant of the right Cauchy-Green tensor $\mathbf{C}_e = \mathbf{G}_e^T \mathbf{G}_e$, and $A_e = \det(\mathbf{G}_e)$ is the relative area change.

$$\lambda_e = v \frac{f_E(d_e)}{(1+v)(1-2v)}, \quad \mu_e = \frac{f_E(d_e)}{2(1+v)}$$

are the Lamé’s first parameter and the shear modulus respectively. Both are influenced by the design function $d(\cdot)$. Note that the maximal elastic energy among all relevant frames is employed here.



By the distribution of elastic energy W_e (see the figure in the right), we segment the entire design domain into the soft and firm regions by the self-tuning spectral clustering method [Zelnik-Manor and Perona 2004] so that different types of microstructures can be assigned into these regions respectively (ref. [Liu et al. 2023b]). When fabricating the braces with the same super-elastic material (i.e., silicone in our trials), we leverage the strength and stiffness of the microstructures type with high-stiffness in the region with low elastic energy and meanwhile also benefit from the flexible deformation characteristics of the type with low-stiffness in the region with high elastic energy. The following section will introduce details about generating distributed microstructures with different stiffness.

4 DISTRIBUTED MICROSTRUCTURES

4.1 Periodical formulation

Different types of microstructures can be represented with the help of an implicit function $f_{\text{cell}}(\hat{u}, \hat{v})$ defined as the distance field to the skeletons in a unit parametric domain $(\hat{u}, \hat{v}) \in [0, 1] \times [0, 1]$. The implicit solid of the distributed microstructures in the domain with design variable $d(u, v)$ can be formulated by a periodic function as

$$f_M(u, v) = d(u, v) - f_{\text{cell}}(\hat{u}, \hat{v}) \quad (5)$$

with $\hat{u} = \arccos(\cos 2u\pi/s)/\pi$, $\hat{v} = \arccos(\cos 2v\pi/s)/\pi$, and s being the scale coefficient of an unit cell in the u, v -domain. The implicit solid of distributed microstructure can then be obtained as $\{(u, v) | f_M(u, v) \leq 0\}$ – see Fig.5 for five different types of microstructures when $d(u, v) = 0.2$. The value of scale coefficient $s = 0.08$ is determined by experiments and employed in all examples in this paper. Note that the function of volume ratio $f_V(\cdot)$ for different types of microstructures is obtained by sampling different values of d and evaluating the volumes of resultant implicit solids. The function $f_V(\cdot)$ is then approximated by a cubic polynomial.

4.2 Mechanical property

Young’s modulus plays a vital role as it indicates a material’s stiffness and elasticity [Murugan 2020]. Different types of microstructures possess Young’s modulus with a broader range than those

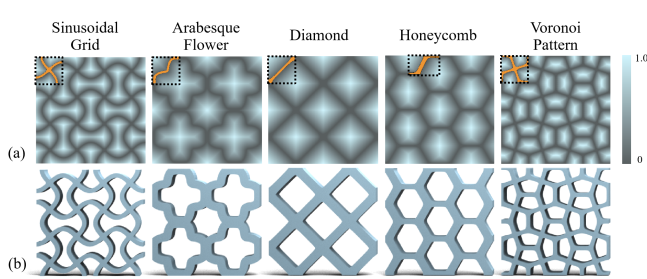


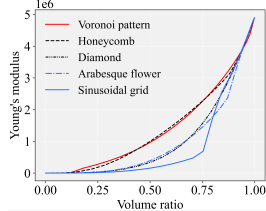
Fig. 5. Different types of microstructures are studied in our research: (a) structures represented by an implicit surface $f_{cell}(\hat{u}, \hat{v})$ in the u, v -domain, and (b) the corresponding solids obtained by $f_{cell}(\hat{u}, \hat{v}) \leq 0.2$ with a user-specified thickness. The function $f_{cell}(\hat{u}, \hat{v})$ is formulated as the distance field to the skeletons (highlighted by curves in orange).

Table 1. Losses for Our Optimization Pipeline

| Loss | Formulation |
|------------------------|---|
| Joint Stability | $\mathcal{L}_1 = \sum_{s \in S_{\text{preserve}}} (\tilde{\phi}_s - \phi_s)^2 + \sum_{s \in S_{\text{prevent}}} \tilde{\phi}_s^2$ |
| Elastic energy density | $\mathcal{L}_2 = \sum_{e=1}^{N_t} W_e$ |
| Compliance | $\mathcal{L}_3 = \frac{1}{2} \left(\sum_{j=1}^{N_t} \left(\sum_{e=1}^{N_t} W_c(d_e, t_i) \right)^p \right)^{\frac{1}{p}}$ |
| Volume fraction | $\mathcal{L}_4 = \left(\sum_{e=1}^{N_t} (f_V(d_e) \cdot V_e) / V_0 - 1 \right)^2$ |
| Seam Continuity | $\mathcal{L}_5 = \sum_{(i,j) \in \mathcal{D}} (d_i - d_j)^2$ |
| Total Loss | $\mathcal{L}_{\text{total}} = \omega_1 \mathcal{L}_1 + \omega_2 \mathcal{L}_2 + \omega_3 \mathcal{L}_3 + \omega_4 \mathcal{L}_4 + \omega_5 \mathcal{L}_5$ |

of conventional materials, which fit well for the design purpose of prophylactic braces.

Young's modulus for microstructures can be approximated by homogenized elasticity tensors. We have evaluated Young's modulus of five types of microstructures shown in Fig.5 by the method presented in [Körner and Liebold-Ribeiro 2014]. Curves between Young's modulus and volume ratio are generated, as shown on the right. It can be observed that the *Voronoi Pattern* structure contains the highest Young's modulus with the same volume ratio, whereas the *Sinusoidal Grid* structure gives the lowest Young's modulus. Following the strategy adopted in [Watts et al. 2019], we use a cubic polynomial function to fit Young's modulus function $f_E(\cdot)$ depending on the design variable d . The resultant continuous and homogeneous Young's modulus functions for both the soft and the firm microstructures are then applied to conduct FEA in Eq.(2) for design optimization, where the volume constraint is controlled with the help of the function $f_V(\cdot)$.



4.3 Blending dual microstructures

After segmenting the design domain of a brace into soft and firm regions with the help of elastic energy obtained by Eq.(4), we generate a blending map $f_{seg}(u, v)$ by assigning $f_{seg}(u, v) = 0$ for the soft region and $f_{seg}(u, v) = 1$ for the firm region. To ensure a smooth

Table 2. List of symbols employed in the loss functions

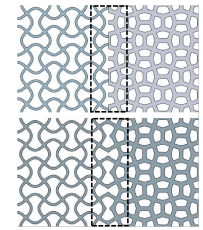
| Term | Explanation |
|-----------------------|--|
| S_{preserve} | Set of DoFs that need to be preserved (e.g. sagittal angles) |
| S_{prevent} | Set of DoFs that need to be controlled (e.g. frontal angles) |
| ϕ_s | Updated joint angle for s given the reaction as defined in Eq.(3) |
| ϕ_s^* | The target joint angle for s |
| W_e | The elastic energy on an element e as defined in Eq.(4) |
| p | The parameter for p -norm method ($p = 20$ in our trials) |
| \mathcal{D} | The pairs of corresponding points on the cutting line |
| d_i | The value of design variable on the i -th node of the mesh \mathcal{M} |
| d_e | The design variable sampled at the center of an element e |

transition, the values of $f_{seg}(u, v)$ at the boundary between soft and firm regions are smoothed by a Laplacian filter. Then, the implicit solid can be defined by blending as

$$f_{\bar{M}}(u, v) = (1 - f_{seg}(u, v))f_{M,s}(u, v) + f_{seg}(u, v)f_{M,f}(u, v) \quad (6)$$

where $f_{M,s}(u, v)$ and $f_{M,f}(d, u, v)$ are the functions of the soft and firm microstructures respectively.

The right figure shows the comparison with (bottom) vs. without (top) the blending formulation. Note that the width of the blended region needs to be controlled because of the inaccuracy of Young's modulus given by the blended microstructures. The microstructures as a distribution optimized on a brace can also be seen on the right side of Fig. 2. The resultant solid can be obtained by first extracting a mesh with $f_M(u, v) \leq d$ on the human body surface and then thickening the surface mesh into a solid [Wang and Chen 2013].



5 LOSS FUNCTIONS

Our optimization model aims to minimize the total elastic energy and compliance with reference to the acting force while considering the joint stability under the prescribed volume fraction. We define each loss term in Table 1 where the definition of relevant symbols are listed in Table. 2. The total loss is defined by combining all terms that are normalized by their initial loss values.

This approach allows us to consider supportiveness and motion flexibility on a brace design concurrently. For practical implementation, seam continuity is considered by maintaining consistent design variables at both sides of a cutting line. Additionally, we incorporate volume fracture loss for the lightweight nature of braces. Note that we only observed a very trivial discontinuity of $d(\cdot)$ across the cutting line in all examples if not applying this loss. However, the value of compliance loss \mathcal{L}_3 will be increased if the discontinuity is not penalized. Therefore, a very small weight $\omega_5 = 0.02$ is employed for the seam continuity loss while the other weights are chosen by experiments as $\omega_1 = 0.5$, $\omega_2 = 0.8$, $\omega_3 = 0.6$ and $\omega_4 = 0.3$.

6 NETWORK ARCHITECTURE

The aim behind introducing neural networks to present the distributed microstructures is to create a differentiable design function

685 $d(\cdot)$ for a gradient-based optimizer. Specifically, $d(\cdot)$ is defined as a
 686 single layer neural-network:

$$687 \quad d(w_1, w_2, \dots, w_{N_w}) = \sum_i^{N_w} w_i \psi_i(u, v), \quad \sum_i^{N_w} w_i = 1 \quad (7)$$

690 with N_w being the number of neurons. The neural weights $\{w_i\}$
 691 are the variables of the optimizer to influence terms defined in the
 692 loss function while serving as the differentiable representation for
 693 microstructures. In our implementation, the Gaussian covariance
 694 $\psi_i(u, v) = \exp(-\sigma^2((u - u_i)^2 + (v - v_i)^2))$ with $\sigma = 4.0$ is chosen
 695 as the activation function because of its high flexibility and adaptability
 696 to non-linear data distributions. The centers of activation
 697 functions are obtained by uniformly sampling the u, v -domain into
 698 N_w points. In addition, the projection is placed behind the single
 699 layer NN in order to keep the design function d within the range
 700 $[0, 1]$. For the sake of easy to converge, a single layer NN is employed
 701 in our implementation with $N_w = 10,000$ neurons.

7 RESULTS AND VALIDATION

We demonstrate our pipeline by analyzing and designing solutions tailored for different joint conditions and varied movement patterns. We fabricate the braces with Silicon rubber with 30A stiffness and verify their performance via physical try-on.

7.1 Design for Prophylactic Braces and Ablation Study

We first design a pair of knee prophylactic braces for tennis serving motion (see Fig. 1 and Fig. 9(a)). During tennis serving that includes the phases of deep knee bending, jumping, and landing, a tennis player can exert forces (normalized by the body weight) on their joints as shown in the force plots of Fig. 1. In the second example, we analyze the kinetics and design bilateral knee braces for gait (see Fig. 9(b)) as it is one of the most common activities in daily life. Our optimizer effectively considers the asymmetry of the body and provides targeted support at the lateral of the knee joint for both sides. In the other example, as different loads are applied to different joints, we also analyze the dynamics of the ankle for a tennis serving motion to generate customized ankle braces as shown in Fig. 9(c).

Furthermore, ablation studies have been conducted to illustrate the necessity of using loss terms. The comparison and analysis are given in Fig. 6. In short, the compliance loss \mathcal{L}_3 is important to provide enough support by controlling the frontal angle, and the loss of elastic energy \mathcal{L}_2 can help effectively keep the flexibility in the sagittal plane. Removing the compliance loss \mathcal{L}_3 will generate a brace without direct connection (by high-density regions) between the upper loop and the lower loop of the brace – i.e., not enough support. On the other aspect, extra high-density regions creating extra restriction to the movement will be given by the design without the loss of elastic energy \mathcal{L}_2 . All these differences in the pattern topology of high-density regions are visualized in Fig. 6.

7.2 Physical Try-on

We fabricated the prophylactic braces for the left knee joint tailored to tennis-serving motion with silicone. Given the body surface of the scanned participant as Fig. 7(a), we obtain the shape parameters, β of the SKEL [Keller et al. 2023] model by optimizing the parameters

Table 3. Joint angle comparison for physical verification at bending and landing moments

| Brace condition | Bending Sagital [†] | Bending Frontal [‡] | Landing Sagital [†] | Landing Frontal [‡] |
|------------------------|------------------------------|------------------------------|------------------------------|------------------------------|
| Unbraced * | 0 | 0.825 | 0 | 16.519 |
| Unoptimized brace | 144.148 | 1.782 | 72.579 | 2.315 |
| Commercial brace | 44.788 | 0.076 | 15.478 | 0.200 |
| Optimized brace (ours) | 1.374 | 0.526 | 0.052 | 1.310 |

[†] Sagittal angle with extension (+) and flexion (-) is compared with *. A sagittal angle close to unbraced condition suggests angle preservation.

[‡] Frontal angle with adduction (+) and abduction (-) is compared with zero. A frontal angle close to zero is indicative of more joint stability within frontal plane.

with a template human body to minimize the distance between two mesh surfaces. We conduct optimization on the SKEL model (β, q), where q is given from the MoCap dataset [Han et al. 2023]. Our optimized design conforms to the scanned body during physical try-on. The comparison of the scanned surface and fitted SKEL is shown in Fig. 3(c) and the detailed fabrication and try-on process can be found in Fig. 7(c, d).

7.3 Verification

While the software solution for simulating the musculoskeletal model with the optimized brace model with distributed microstructures is not publicly accessible, we directly conduct physical experiments to validate the performance of optimized braces generated by our approach (see Fig. 8). We test the fabricated left knee brace for a tennis player and evaluate the joint angles from the mocap data obtained from performing tennis serving movements. Our optimized design is compared against unbraced conditions, wearing unoptimized and commercial braces, as shown in Fig. 8. We demonstrate that the braces with the optimized distribution of elasticity can help reduce the risk of injury by preserving the flexibility of movement within the sagittal plane (Column 1, 3 from Table. 3) while reducing the frontal angles (Column 2, 4 from Table. 3).

8 CONCLUSION AND DISCUSSION

We present a motion-driven neural optimizer that leverages biomechanical insights and physical formulation for the topology design of prophylactic braces tailored to human motions. The results generated by our pipeline are very encouraging. Tailor-made mechanical protection and preservation were observed in the experiments of physical verification on the optimized braces.

Our approach has several limitations that should be acknowledged. First, the mesh density and quality used for FEA could impact the accuracy of the simulation results. Additionally, the shape of the brace is derived from a human body model created by fitting a SKEL model onto a scan, which may introduce errors. Furthermore, the study simplifies the analysis by neglecting FEA on bone structures and not accounting for changes in muscle forces due to reaction forces generated by different brace elasticities. These simplifications and potential errors could influence the accuracy and prevent the generation of further optimized braces. Future work should address these limitations to improve the precision of the results.

REFERENCES

- Michael Skipper Andersen and John Rasmussen. 2023. Chapter 7 - AnyBody modeling system. In *Digital Human Modeling and Medicine*, Gunther Paul and Mohamed Hamdy Doweidar (Eds.). Academic Press, 143–159. <https://doi.org/10.1016/B978-0-12-823913-1.00007-5>
- Bruno Luiz Souza Bedo, Danilo S Catelli, Mario Lamontagne, and Paulo Roberto Pereira Santiago. 2020. A custom musculoskeletal model for estimation of medial and lateral tibiofemoral contact forces during tasks with high knee and hip flexions. *Computer methods in biomechanics and biomedical engineering*. 23, 10 (2020).
- Javier Bonet and Richard D Wood. 2008. *Nonlinear Continuum Mechanics for Finite Element Analysis*. Cambridge University Press. <https://doi.org/10.1017/CBO97805117554464>
- Jinhui Cai, Long Huang, Hongyu Wu, and Lairong Yin. 2023. Concurrent topology optimization of multiscale structure under uncertain dynamic loads. *International Journal of Mechanical Sciences* 251 (2023), 108355. <https://doi.org/10.1016/j.ijmecsci.2023.108355>
- Aaditya Chandrasekhar and Krishnan Suresh. 2021. TOUNN: Topology optimization using neural networks. *Structural and Multidisciplinary Optimization* 63, 3 (2021), 1135–1149.
- Desai Chen, Mélina Skouras, Bo Zhu, and Wojciech Matusik. 2018. Computational discovery of extremal microstructure families. *Science advances* 4, 1 (2018), eaao7005.
- Scott L Delp, Frank C. Anderson, Allison S. Arnold, Peter Loan, Ayman Habib, Chand T. John, Eran Guendelman, and Darryl G. Thelen. 2007. OpenSim: Open-Source Software to Create and Analyze Dynamic Simulations of Movement. *IEEE Transactions on Biomedical Engineering* 54, 11 (2007), 1940–1950. <https://doi.org/10.1109/TBME.2007.901024>
- Kelley E. Farwell, Cameron J. Powden, Meaghan R. Powell, Cailee W. McCarty, and Matthew C. Hoch. 2013. The Effectiveness of Prophylactic Ankle Braces in Reducing the Incidence of Acute Ankle Injuries in Adolescent Athletes: A Critically Appraised Topic. *Journal of Sport Rehabilitation* 22, 2 (2013), 137–142. <https://doi.org/10.1123/jsr.22.2.137>
- Yusen Feng, Xiyuan Xu, and Libin Liu. 2023. MuscleVAE: Model-Based Controllers of Muscle-Actuated Characters. In *SIGGRAPH Asia 2023 Conference Papers (SA '23)*. Association for Computing Machinery, New York, NY, USA, Article 3, 11 pages. <https://doi.org/10.1145/3610548.3618137>
- Michael T. Gross and Hsin-Yi Liu. 2003. The Role of Ankle Bracing for Prevention of Ankle Sprain Injuries. *Journal of Orthopaedic & Sports Physical Therapy* 33, 10 (2003), 572–577. <https://doi.org/10.2519/jospt.2003.33.10.572>
- Austin Hagan, Diana Rocchio, Jaeho Shim, Jonathan Rylander, and Darryn Willoughby. 2024. Effects of Prophylactic Lace-Up Ankle Braces on Kinematics of the Lower Extremity During a State of Fatigue. *International Journal of Kinesiology and Sports Science* 12, 1 (2024). <https://doi.org/10.7575/aiac.ijkss.v.12n.1p.24>
- Xingjian Han, Benjamin Senderling, Stanley To, Deepak Kumar, Emily Whiting, and Jun Saito. 2023. GroundLink: A Dataset Unifying Human Body Movement and Ground Reaction Dynamics. In *ACM SIGGRAPH Asia 2023 Conference Proceedings*, 1–10.
- Jakob S Jensen. 2009. Space-time topology optimization for one-dimensional wave propagation. *Computer Methods in Applied Mechanics and Engineering* 198, 5–8 (2009), 705–715.
- Jingchao Jiang, Yi Xiong, Zhiyuan Zhang, and David W Rosen. 2022. Machine learning integrated design for additive manufacturing. *Journal of Intelligent Manufacturing* 33, 4 (2022), 1073–1086.
- Marilyn Keller, Keenon Werling, Soyong Shin, Scott Delp, Sergi Pujades, C. Karen Liu, and Michael J. Black. 2023. From Skin to Skeleton: Towards Biomechanically Accurate 3D Digital Humans. In *ACM ToG, Proc. SIGGRAPH Asia*, Vol. 42.
- Carolin Körner and Yvonne Liebold-Ribeiro. 2014. A systematic approach to identify cellular auxetic materials. *Smart Materials and Structures* 24, 2 (2014), 025013.
- Zachary F. Lerner, Matthew S. DeMers, Scott L. Delp, and Raymond C. Browning. 2015. How tibiofemoral alignment and contact locations affect predictions of medial and lateral tibiofemoral contact forces. *Journal of Biomechanics* 48, 4 (2015), 644–650. <https://doi.org/10.1016/j.jbiomech.2014.12.049>
- Bruno Lévy, Sylvain Petitjean, Nicolas Ray, and Jérôme Maillot. 2023. Least squares conformal maps for automatic texture atlas generation. In *Seminal Graphics Papers: Pushing the Boundaries, Volume 2*. 193–202.
- Baoshou Liu, Xiaoming Wang, Zhuo Zhuang, and Yinan Cui. 2023a. Dynamic concurrent topology optimization and design for layer-wise graded structures. *Composite Structures* 319 (2023), 117190. <https://doi.org/10.1016/j.compositesct.2023.117190>
- Baoshou Liu, Xiaoming Wang, Zhuo Zhuang, and Yinan Cui. 2023b. Dynamic concurrent topology optimization and design for layer-wise graded structures. *Composite Structures* 319 (2023), 117190.
- S Senthil Murugan. 2020. Mechanical properties of materials: definition, testing and application. *Int. J. Mod. Stud. Mech. Eng* 6, 2 (2020), 28–38.
- Gregory D Myer, Kevin R Ford, Jane Khouri, Paul Succop, and Timothy E Hewett. 2011. Biomechanics laboratory-based prediction algorithm to identify female athletes with high knee loads that increase risk of ACL injury. *British Journal of Sports Medicine* 45, 4 (2011), 245–252. <https://doi.org/10.1136/bjsm.2009.069351>
- Wenliang Qian, Yang Xu, and Hui Li. 2023. A topology description function-enhanced neural network for topology optimization. *Computer-Aided Civil and Infrastructure Engineering* 38, 8 (2023), 1020–1040.
- Arash Radman, Xiaodong Huang, and YM Xie. 2013. Topology optimization of functionally graded cellular materials. *Journal of Materials Science* 48 (2013), 1503–1510.
- Ole Sigmund. 1994. Materials with prescribed constitutive parameters: an inverse homogenization problem. *International Journal of Solids and Structures* 31, 17 (1994), 2313–2329.
- Ole Sigmund. 2001. A 99 line topology optimization code written in Matlab. *Structural and multidisciplinary optimization* 21 (2001), 120–127.
- Saketh Sridhara, Aditya Chandrasekhar, and Krishnan Suresh. 2022. A generalized framework for microstructural optimization using neural networks. *Materials & Design* 223 (2022), 111213.
- Robert W Sumner and Jovan Popović. 2004. Deformation transfer for triangle meshes. *ACM Transactions on graphics (TOG)* 23, 3 (2004), 399–405.
- Salvatore Torquato. 2010. Optimal design of heterogeneous materials. *Annual review of materials research* 40 (2010), 101–129.
- Brian H. H. Tuang, Zheng Qin Ng, Joshua Z. Li, and Dinesh Sirisena. 2023. Biomechanical Effects of Prophylactic Knee Bracing on Anterior Cruciate Ligament Injury Risk: A Systematic Review. *Clinical Journal of Sport Medicine* 33, 1 (January 2023), 78–89. <https://doi.org/10.1097/JSM.0000000000001052>
- Velko Vechev, Ronan Hinche, Stelian Coros, Bernhard Thomaszewski, and Otmar Hilliges. 2022a. Computational Design of Active Kinesthetic Garments. In *Proceedings of the 35th Annual ACM Symposium on User Interface Software and Technology* (Bend, OR, USA) (UIST '22). Association for Computing Machinery, New York, NY, USA, Article 23, 11 pages. <https://doi.org/10.1145/3526113.3545674>
- Velko Vechev, Ronan Hinche, Stelian Coros, Bernhard Thomaszewski, and Otmar Hilliges. 2022b. Computational Design of Active Kinesthetic Garments. In *Proceedings of the 35th Annual ACM Symposium on User Interface Software and Technology*. 1–11.
- Velko Vechev, Juan Zarate, Bernhard Thomaszewski, and Otmar Hilliges. 2022c. Computational design of kinesthetic garments. In *Computer Graphics Forum*, Vol. 41. Wiley Online Library, 535–546.
- E A L M Verhagen and K Bay. 2010. Optimising ankle sprain prevention: A critical review and practical appraisal of the literature. *British Journal of Sports Medicine* (2010). <https://doi.org/10.1136/bjsm.2010.076406>
- Charlie C.L. Wang and Yong Chen. 2013. Thickening freeform surfaces for solid fabrication. *Rapid Prototyping Journal* 19, 6 (2013), 395–406.
- Charlie C.L. Wang and Kai Tang. 2007. Woven model based geometric design of elastic medical braces. *Computer-Aided Design* 39, 1 (2007), 69–79.
- Weiming Wang, Dirk Munro, Charlie CL Wang, Fred van Keulen, and Jun Wu. 2020. Space-time topology optimization for additive manufacturing: Concurrent optimization of structural layout and fabrication sequence. *Structural and Multidisciplinary Optimization* 61 (2020), 1–18.
- Seth Watts, William Arrighi, Jun Kudo, Daniel A Tortorelli, and Daniel A White. 2019. Simple, accurate surrogate models of the elastic response of three-dimensional open truss micro-architectures with applications to multiscale topology design. *Structural and Multidisciplinary Optimization* 60 (2019), 1887–1920.
- Keenon Werling, Nicholas A. Bianco, Michael Raitor, Jon Stingel, Jennifer L. Hicks, Steven H. Collins, Scott L. Delp, and C. Karen Liu. 2023. Ad-Biomechanics: Automating model scaling, inverse kinematics, and inverse dynamics from human motion data through sequential optimization. *bioRxiv* (2023). <https://doi.org/10.1101/2023.06.15.545116> arXiv:<https://www.biorxiv.org/content/early/2023/09/08/2023.06.15.545116.full.pdf>
- Jonas Zehnder, Yue Li, Stelian Coros, and Bernhard Thomaszewski. 2021. Ntopo: Mesh-free topology optimization using implicit neural representations. *Advances in Neural Information Processing Systems* 34 (2021), 10368–10381.
- Lihui Zelnik-Manor and Pietro Perona. 2004. Self-tuning spectral clustering. *Advances in neural information processing systems* 17 (2004).
- Yunbo Zhang and Tsz-Ho Kwok. 2019. Customization and topology optimization of compression casts/braces on two-manifold surfaces. *Computer-Aided Design* 111 (2019), 113–122.
- Zeyu Zhang, Yu Li, Weien Zhou, Xiaoqian Chen, Wen Yao, and Yong Zhao. 2021. TONR: An exploration for a novel way combining neural network with topology optimization. *Computer Methods in Applied Mechanics and Engineering* 386 (2021), 114083.
- Bo Zhu, Mélina Skouras, Desai Chen, and Wojciech Matusik. 2017. Two-scale topology optimization with microstructures. *ACM Transactions on Graphics (TOG)* 36, 4 (2017), 1.

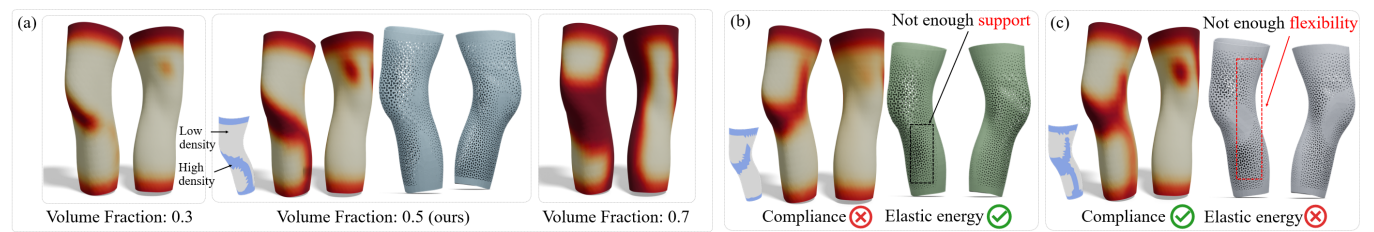


Fig. 6. Ablation study for the necessity of different loss terms: (a) The loss term of volume fraction \mathcal{L}_4 is employed to control the amount of materials used for the braces – the volume fraction 0.5 is employed for all other examples in this paper. (b) removing the compliance loss \mathcal{L}_3 will generate a brace with less support to prevent the adduction – the upper & lower loops of the brace are not connected by high-density regions, and (c) the flexibility of movement is not preserved without the loss of elastic energy density \mathcal{L}_2 which leads to a result with extra connection from the knee to the upper loop by a high-density region.

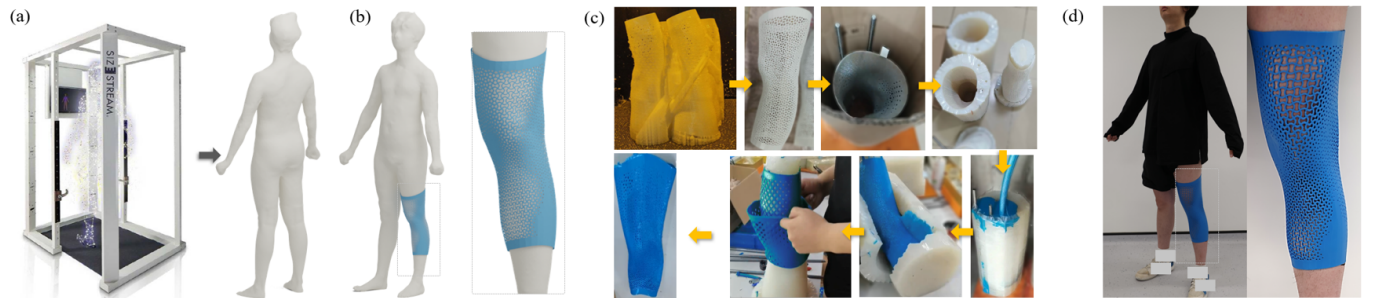
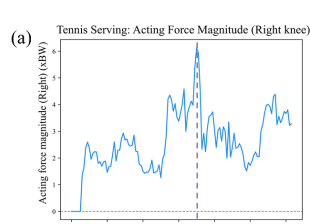


Fig. 7. To ensure the brace can be properly worn, we first capture the participant's body by a structure-light based scanner (online image resource accessed May 2024) and reconstruct the 3D surface (a). The optimized design of a knee brace is computed in a user-specified region (b). The designed brace with microstructures are generated by offsetting and fabricated by Silicon rubber with 30A stiffness using a casting method with the 3D printed mold (c).

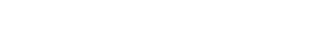
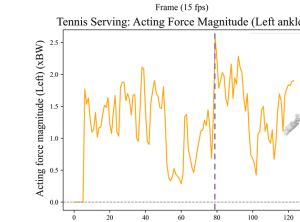
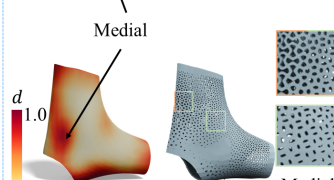
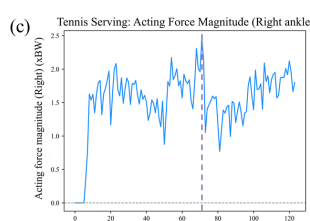
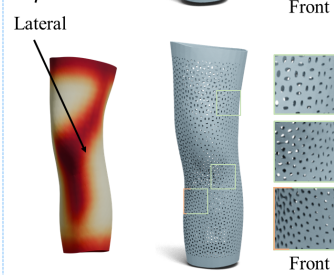
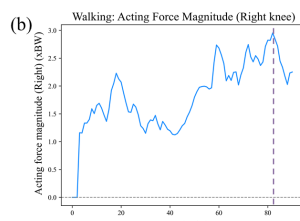
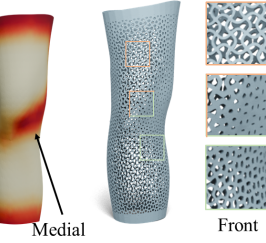


Fig. 8. Physical validation of prophylactic brace for the left knee. Left: (d) Motion capture system with twelve Vicon Vero 13 cameras. (a) Motion capture protocol for 13 markers placed on left lower extremity: 2 clusters on femur and tibia – each with 4 markers (see red boxes), which are used to compute knee angles. Five more calibration markers located on left hip, lateral and medial of left knee and ankle to identify joint and body segments. The participant repeats the tennis serving motion 5 times for (b) unbraced, (c) wearing our optimized brace, (e) a commercial prophylactic brace and (f) an unoptimized brace with uniform ‘Voronoi Pattern’ microstructure. Right: plot of joint angles for comparison. Note the peak flexion is used for alignment and the second peak flexion is selected for comparing the angles for both planes at the landing moment, as this passive action can elevate the risk of joint injury, especially if the knee lacks adequate flexibility and remains extended upon landing. Our optimized design yields similar support as the uniform stiff patterns (reduced) and commercial braces while providing more flexibility within the sagittal plane, which is important to allow more bending upon contact with the ground.

1027

Acting force[†]

Viewing angle 1



Viewing angle 2

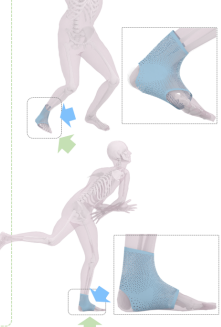
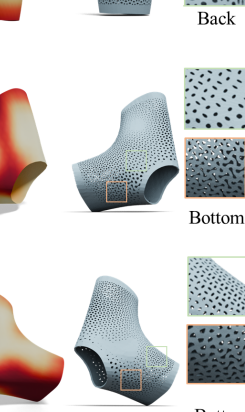
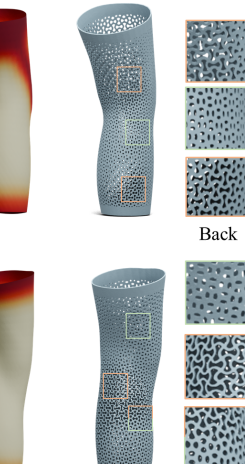
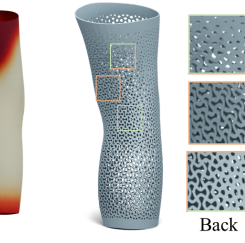


Fig. 9. We present a collection of designed prophylactic braces, demonstrating the capability of the pipeline for designing braces for different joint dynamics and varied movement patterns. The columns are: (far-left) magnitude of time-variant acting force given by the joint contact forces and muscle forces; (second-far-left) peak acting forces on the joint; (middle) optimized design variable field and a detailed view of the braces' distributed microstructures from two different angles; (right) showcase of optimized design on the simulated human body of the same frame. Zoom-in views for firm (green) and soft (orange) regions are marked in boxes. (a) Compared with the left prophylactic knee brace for tennis motion (Fig. 1), we yield different structure designs for the right side due to the asymmetry of human motion and different loads acting on the body. (b) Gait example: our optimizer generates more lateral support on the knee to help stabilize the joint and prevent lateral movement during walking. (c) Landing impact after tennis serve creates higher loads acting on the ankle joint. The designs for the left ankle specifically address the impact of bending and landing motions, which can significantly increase the risk of ankle injuries. The design result aims to provide protection for the medial sides of the foot that aims to mitigate eversion angles. ([†]The magnitude of the acting force are plotted.)

1084

1085

1086

1087

1088

1089

1090

1091

1092

1093

1094

1095

1096

1097

1098

1099

1100

1101

1102

1103

1104

1105

1106

1107

1108

1109

1110

1111

1112

1113

1114

1115

1116

1117

1118

1119

1120

1121

1122

1123

1124

1125

1126

1127

1128

1129

1130

1131

1132

1133

1134

1135

1136

1137

1138

1139

1140